Electrochimica Acta 186 (2015) 494–503

Contents lists available at ScienceDirect

Electrochimica Acta

journal homepage: www.elsevier.com/locate/electacta

# Optimal dose-response relationship in electrolytic ablation of tumors with a one-probe-two-electrode device

E. Luján[a,b,d,e,1], H. Schinca[a,1], N. Olaiz[a,b,e], S. Urquiza[d], F.V. Molina[c], P. Turjanski[a,e], G. Marshall[a,b,e,*]

[a] Laboratorio de Sistemas Complejos, Departamento de Computación, Facultad de Ciencias Exactas y Naturales, Universidad de Buenos Aires, Argentina
[b] Instituto de Física del Plasma, Facultad de Ciencias Exactas y Naturales, Universidad de Buenos Aires, Argentina
[c] Instituto de Química Física de los Materiales, Medio Ambiente y Energía, Departamento de Química, Facultad de Ciencias Exactas y Naturales, Universidad de Buenos Aires, Argentina
[d] Grupo de Ingeniería Asistida por Computadora, Facultad de Ingeniería, Universidad Nacional de Mar del Plata, Argentina
[e] Consejo Nacional de Investigaciones Científicas y Técnicas, Argentina

ARTICLE INFO

*Article history:*
Received 28 June 2015
Received in revised form 22 October 2015
Accepted 24 October 2015
Available online 28 October 2015

*Keywords:*
Tumors
Electrolytic ablation
Electrochemical treatment
*in silico* models
*in vitro* models
pH front tracking

ABSTRACT

Electrolytic ablation (EA), a medical treatment used in solid tumor ablation due to its minimum side effects and low cost, consists in the passage of a low constant electric current through two or more electrodes inserted in the tissue thus inducing pH fronts that produce tumor necrosis. Combined with a recently introduced one-probe two electrode device (OPTED) this procedure results in a minimally invasive treatment. Despite its success, EA has drawbacks such as the difficulties in determining the optimum dose-response relationship between the applied current, treatment time and necrotized tumor volume (NTV) and choosing a reliable dose parameter. In this work, a theoretical model is introduced describing the EA/OPTED as an electrolytic process and the underlying electrochemical reactions through the Nernst-Planck equations for ion transport. Model results show that the coulomb dosage is a reliable dose parameter and predicts an optimal dose-response relationship for a given tumor size subjected to an EA/OPTED, considering the optimum as the minimum coulomb dosage necessary to achieve total tumor destruction while minimizing healthy tissue damage. Moreover, it predicts a nonlinear relationship between coulomb dosage and NTV, dosage and NTV scaling as $Q^{1.4}$. Consequently, these results could have a significant impact on dose planning methodology aimed at improving the effectiveness of the electrolytic ablation.



## 1. Introduction

Electrolytic ablation (EA) of tumors, also called electrochemical treatment of tumors (EChT), is a non-thermal ablative method consisting in the application of a low direct electric current through two or more electrodes inserted in the tissue generating electrolytic products that induces tumor necrosis. This treatment was pioneered by Nordenström [1,2] and has been widely used in China with good clinical results [3,4]. In [5–8] the effects of EA in tumors in mice, either alone or with the use of chemotherapy, were studied. During the last decade, pulsed electric fields were explored in local tumor treatment based upon electroporation (EP), a technique in which pulsed electric fields are employed to perturb cell membrane permeability. Among them, electrochemotherapy (ECT) combines reversible EP with poorly-permeant anticancer drugs to potentiate their entry to the cell thus their intrinsic cytotoxicity. Since its beginnings in the late 1980s, ECT has evolved into a clinically verified efficient treatment for tumors of different origin in Europe [9,10]. Recently, in [11] it was shown that combining EA with reversible EP yields a significant increase in the extent of tissue ablation in comparison to that obtained with EA alone. A possible explanation is that reversible EP potentiates the entrance of toxic electrolytic products into the cell increasing NTV. NTV is defined as the volume of the tumor necrotized by EA. In summary, whether alone or combined with EP, some of the advantages of EA are its simplicity, effectiveness, and negligible side effects.

Tissue destruction in EA is mainly produced by necrosis. This is because, during the electrolysis process, electrochemical reactions take place at the electrodes, producing at the anode oxygen, chlorine and protons as the main byproducts, while hydrogen and hydroxide ions are released at the cathode.

* Corresponding author. Tel.: +54 11 4576 3390 ext.709;fax: +54 11 4576 3359.
*E-mail address:* marshalg@retina.ar (G. Marshall).
[1] These two authors contributed equally to this work..

http://dx.doi.org/10.1016/j.electacta.2015.10.147
0013-4686/

It is the presence of strong pH changes that causes necrosis. Concomitantly, there is a migration displacement of water from the anode to the cathode causing dryness at the former and hydration at the latter. Part of the gasses released at the electrodes remain present in the medium and participate in other chemical reactions with organic and inorganic components of the tissue [12].

In spite of the wide clinical experience available, still there is a need for a deeper understanding of the fundamental mechanisms involved in EA. Mathematical modeling validated with experimental measurements can greatly contribute to this goal. In a pioneering series of papers [12–16], *in silico* modeling of an EA protocol applied to a tumor tissue were presented. The tissue matrix was seen as an electrolyte and the EA protocol as an electrolysis process. The ion transport in a zone near one of the electrodes (cathode or anode) was described by a quasi-three-dimensional model (spherical symmetry model) using the Nernst-Planck equations for ion transport. Results show pH profiles at the anode to be strongly correlated with the size of *in vitro* measured necrosis, thus confirming the effect of pH (the spreading of hydroxyl ions) in tissue necrosis and suggesting that the model could be used for predicting EA tumor treatment. More realistic models were presented in [17] and [18] solving the one-dimensional Nernst-Planck equations for ion transport in which the full cathode-anode ion transport interaction was described. Results show that under EA modeling with two electrodes (with a separation of 3 cm between them), an initial condition with almost neutral pH evolves between electrodes into extreme cathodic alkaline and anodic acidic fronts moving towards each other, leaving the possible existence of a biological pH region between them; towards the periphery, the pH decays to its neutral values. Moreover, results also suggested that since necrotic areas correlated well with those covered by alkaline and acid fronts advances, pH front tracking can be effectively used to predict the extent of tumor destruction and thus, the assessment of EA effectiveness.

In [19] a one-probe two-electrode device (OPTED) containing the cathode and the anode very close to each other ($10^{-3}m$) was introduced; its main advantage under an EA protocol is the insertion of one applicator rather than two or more, thus minimizing tissue intrusion. Experiments show that upon application of the EA/OPTED protocols in a 3D gel model, two half-spherical pH fronts, one basic and the other acid (from cathode and anode, respectively), expand towards the periphery configuring a distorted full sphere. Between electrodes, the fronts collide and vanish due to neutralization. The efficacy of the EA/OPTED protocol was assessed measuring the extent of the necrotized area. This was determined by the area covered by acid fronts through a pH front tracking using pH color change indicators.

Dose planning methodology is mandatory for a reliable treatment outcome. Since the late seventies coulomb dosage (defined as the electric charge, that is, the intensity of the constant electric current applied multiplied by the time of its application) according to tumor size was the guideline for optimal choice of electric parameters [20]. Later on, searching for optimal dose planning, several authors investigated the dose-response relationship between the applied current, treatment time, coulomb dosage and NTV. Some authors [20] used different coulomb dosages and found a linear relationship between NTV and coulomb dosage (this was also experimentally corroborated in [17] though this result was not checked with a theoretical model). They also found no differences using lower or higher currents at a given coulomb dosage. Though these results seem to imply that coulomb dosage is a reliable parameter other authors [20] found NTV to be related, not only to coulomb dosage but also to the way at which it was administered. Low current and longer treatment times yielded higher NTV, compared with higher current and shorter treatment time [21]. Given these controversial results, the problem as to whether the coulomb dosage is a reliable dose parameter remains open.

The goal of this work is to establish the coulomb dosage as a reliable dose parameter and to determine the optimal dose-response relationship for a given tumor size subject to an EA/OPTED, that is, the coulomb dosage necessary to achieve total NTV while minimizing healthy tissue damage. This is obtained through mathematical modeling validated with experimental measurements.

The plan of the paper follows: Section 2, Material and methods, presents *In vitro* modeling and *In silico* modeling, Section 3, presents results of *in vitro* modeling and *in silico* modeling and a comparison between them and discussions, finally Section 4, presents general conclusions.

## 2. Materials and methods

### 2.1. In vitro *modeling*

*In vitro* modeling of the EA/OPTED protocol in a 3D gel cube is described in detail in [19]. Here we present a summary. As shown in Fig. 1(a) the tissue is represented by a gel cube ($0.023\ m \times 0.023\ m \times 0.018\ m$) consisting of 1% agar-agar in distilled water, with *NaCl* at physiological concentration ($160\ mol/m^3$). The OPTED is composed of two parallel needles separated $10^{-3}m$ from each other, and encased in a truncated cone holder, whose top and bottom diameters are $2\ 10^{-3}m$ and $5\ 10^{-3}m$, respectively (the holder has a length slightly larger than half of the gel cube width). Each needle is electrically insulated except at the point where it is in contact with the gel, thus the electrode. Each electrode has an exposed area of $1.5\ 10^{-7}\ m^2$. The OPTED is inserted in the middle of the cube back face. In [19] a constant current (taking the values: $4\ 10^{-3}A$, $8\ 10^{-3}A$ and $10\ 10^{-3}A$) was applied during 1200 *s*. The applied voltage ranged from 3.9 V at $2\ 10^{-3}A$ to 5.1 *V* at $10^{-2}A$. pH front tracking was done via an optical absorption technique. Phenolphthalein ($C_{20}H_{14}O_4$, transition pH range 8.0 - 9.62) and methyl red ($C_{15}H_{16}N_3O_2Cl$, transition pH range 4.8 - 6.2) were used as basic and acid indicators, respectively. Electric current circulation between the two electrodes in an electrolyte produces bubbles. If the electrodes are close enough, bubbles between them act as an electric insulator, diminishing the effective area through which electric current flows and increasing the current density.

### 2.2. In silico *modeling*

EA/OPTED therapy is an evolutionary process determined by the products emerging from the electrolysis process, in particular, pH fronts which are the main cause of tissue destruction. During the process, all the variables intervening in the electrolysis and in the generation of electrolytic products are modified. Clearly, pH fronts, thus EA/OPTED therapy, is a highly nonlinear process strongly dependent in the transport of ions and in the electrochemical reactions taking place at the electrodes.

Accordingly, for the establishment of the coulomb dosage as a reliable dose parameter and for determining the optimal dose-response relationship for a given tumor size subject to an EA/OPTED, the following *in silico* model describing the underlying ion transport process is introduced.

Assuming that ion transport is solely governed by diffusion and migration the *in silico* EA/OPTED model in a 3D domain is described by the Nernst-Planck equations for the concentration of ions in a four component electrolyte where Butler-Volmer and electroneutrality conditions prevail. Thermal effects are not taken into account in our model because they are considered negligible vis-à-vis pH fronts effects. The model comprises four unknown variables: the concentrations of $B = H^+$, $OH^-$, $Cl^-$, $Na^+$ ions. In passing, it is worth

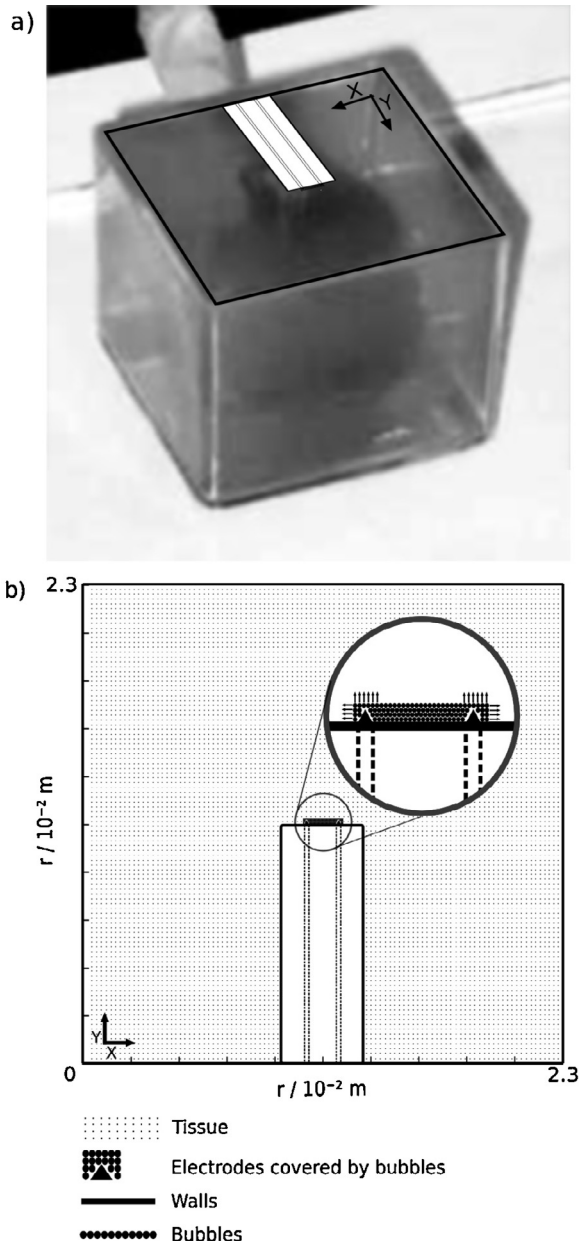


**Fig. 1.** a) Snapshot of a fully developed spherical pH fronts halo emerging from the OPTED electrode (inserted normally to the center of the back face of the gel cube) during an EA/OPTED (image modified from a figure taken from [19]). b) The computational domain in the x-y plane (rotated top view of the cube and the OPTED electrode). The zoomed region at the top right corner displays bubbles surrounding electrodes.

noting that tissue natural buffer plays a role in the dose-response relationship as it tends to neutralize pH fronts. However, it is not taken into account in the present model because of the working conditions used: the rate of protons and hydroxyl generation at the electrodes quickly overcomes the buffering capability of the tissue fluids. The equations are written as:

$$\frac{\partial C_B}{\partial t} + \nabla \cdot \boldsymbol{N_B} = R_B \tag{1}$$

Here, the molar flux is:

$$\boldsymbol{N_B} = -D_B \nabla C_B - \frac{z_B}{|z_B|} u_B C_B \nabla \Phi \tag{2}$$

where $D_B$, $C_B$, $z_B$ and $u_B$ are the diffusion coefficient, concentration, charge number (with sign) and mobility of the species $B$, $\Phi$ is the electric potential and $t$ is the time.

The ionic mobility and diffusion coefficient are related through the Nernst-Einstein equation:

$$D_B = \frac{RT}{|z_B|F} u_B \tag{3}$$

where $T$ is the absolute temperature, $R$ the universal gas constant and $F$ the Faraday's constant.

$R_B$ represents the production of species $B$ through chemical reactions in the electrolyte. In particular, water proteolysis reaction is the only homogeneous chemical reaction considered:

$$H^+ + OH^- \underset{k_{w,b}}{\overset{k_{w,f}}{\rightleftharpoons}} H_2O$$

where $k_{w,b}$ and $k_{w,f}$ are the backward and forward dissociation constants of water, respectively. The reaction terms in tissue are:

$$R_{H^+} = R_{OH^-} = k_{w,b} C_{H_2O} - k_{w,f} C_{H^+} C_{OH^-} \tag{4}$$

$$R_{Cl^-} = R_{Na^+} = 0 \tag{5}$$

Combining Eqs. (1), (2), (3), (4) and (5)

$$\frac{\partial C_{H^+}}{\partial t} = \nabla \cdot \left(D_{H^+} \nabla C_{H^+} + \frac{z_{H^+}}{|z_{H^+}|} u_{H^+} C_{H^+} \nabla \Phi\right) + k_{w,b} C_{H_2O} - k_{w,f} C_{H^+} C_{OH^-} \tag{6}$$

$$\frac{\partial C_{OH^-}}{\partial t} = \nabla \cdot \left(D_{OH^-} \nabla C_{OH^-} + \frac{z_{OH^-}}{|z_{OH^-}|} u_{OH^-} C_{OH^-} \nabla \Phi\right) + k_{w,b} C_{H_2O} - k_{w,f} C_{H^+} C_{OH^-} \tag{7}$$

$$\frac{\partial C_{Cl^-}}{\partial t} = \nabla \cdot \left(D_{Cl^-} \nabla C_{Cl^-} + \frac{z_{Cl^-}}{|z_{Cl^-}|} u_{Cl^-} C_{Cl^-} \nabla \Phi\right) \tag{8}$$

The concentration of the fourth specie ($Na^+$), is obtained via the electroneutrality condition (9):

$$\sum_B z_B \; C_B = 0 \tag{9}$$

The electrostatic potential $\Phi$ can be calculated from the charge conservation condition

$$\nabla \cdot \boldsymbol{j_T} = 0 \tag{10}$$

where the total current density $\boldsymbol{j_T}$ is given by

$$\boldsymbol{j_T} = F \sum_B z_B \; \boldsymbol{N_B} \tag{11}$$

the electrostatic potential $\Phi$ is obtained from

$$\sum_B z_B \nabla \cdot (D_B \nabla C_B) + \sum_B |z_B| u_B \nabla \cdot (C_B \nabla \Phi) = 0 \tag{12}$$

The electric field is obtained via

$$\boldsymbol{E} = -\nabla \Phi \tag{13}$$

System (1–13) with appropriate initial and boundary conditions (described in the appendix) is valid in a space domain defined by the geometry in Fig. 1(b) and time.

Table 1 presents the parameters used in the model. Published diffusion coefficients of ions in liquid medium [22] were adequately reduced to describe diffusion in a gel medium:

$$D_B^{Gel} \cong 0.8 \; D_B^{Water}$$

**Table 1**
*In silico* model parameters.

| Parameter | Value | Ref | Parameter | Value | Ref |
|---|---|---|---|---|---|
| $z_{H^+}$ | 1 | | $z_{OH^-}$ | −1 | |
| $z_{Cl^-}$ | −1 | | $z_{Na^+}$ | 1 | |
| $D_{H^+}$ | $9.31\ 10^{-9}\ m^2\ s^{-1}$ | | $D_{OH^-}$ | $5.26\ 10^{-9}\ m^2\ s^{-1}$ | |
| $D_{Na^+}$ | $1.33\ 10^{-9}\ m^2\ s^{-1}$ | | $D_{Cl^-}$ | $2.03\ 10^{-9}\ m^2\ s^{-1}$ | |
| $C^0_{H^+}$ | $10^{-4}\ mol\ m^{-3}$ | | $C^0_{OH^-}$ | $10^{-4}\ mol\ m^{-3}$ | |
| $C^0_{Na^+}$ | $160\ mol\ m^{-3}$ | [23] | $C^0_{Cl^-}$ | $160\ mol\ m^{-3}$ | [23] |
| $C^0_{H_2O}$ | $55500\ mol\ m^{-3}$ | | $T$ | $298\ K$ | |
| $F$ | $96485.3415\ A\ s\ mol^{-1}$ | | $R$ | $8.31\ kg\ m^2\ K^{-1}\ mol^{-1}\ s^{-2}$ | |
| $n_{R_{O_2}}$ | 4 | | $n_{R_{Cl_2}}$ | 2 | |
| $n_{H_2,2OH^-}$ | 2 | | $\nu_{H^+,R_{O_2}}$ | 4 | |
| $\nu_{Cl_2,R_{Cl_2}}$ | 2 | | $\nu_{OH^-,R_{H_2,2OH^-}}$ | 2 | |
| $j^{eq}_{R_{O_2}}$ | $10^{-6}\ A\ m^{-2}$ | [24] | $j^{eq}_{R_{Cl_2}}$ | $10\ A\ m^{-2}$ | [25] |
| $E^{eq}_{R_{Cl_2}}$ | $1.407\ V$ | | $E^{eq}_{R_{O_2}}$ | $0.816\ V$ | [22] |
| $k_{w,f}$ | $1.5\ 10^8\ m^3\ mol^{-1}\ s^{-1}$ | [26] | $k_{w,b}$ | $2.7\ 10^{-5}\ s^{-1}$ | [26] |

Diffusion coefficients are given at an infinite dilution in water at 37 ◦ C. *In vitro* experiments [19] show that the pH fronts advance is almost spherical, from the center of the gel cube in the outward direction. Previously published 1D mathematical models [13–16] assumed spherical symmetry, thus they are limited due to the inherent bias between the acid and basic fronts. Accordingly, here we introduce a 2D representation assuming negligible changes in the z-axis, and for this purpose, adapting the effective area of the electrode due to bubble effects and proton diffusion coefficients (see Table 2). Bubbles at the electrodes are not fully described by the model.

Fig. 1(b) shows the scheme of the computational domain (a box of $2.3\ 10^{-2}m \times 2.3\ 10^{-2}m$) used in the x-y plane (rotated top view of the cube and the OPTED). This box is described by a uniform mesh of 10000 nodes (100 × 100). The holder is proxied by a rectangular domain with a diameter of $3.45\ 10^{-3}m$ as shown in the figure. The zoomed region at the top right corner displays the holder top with the protruding electrodes with an exposed area of $1.5\ 10^{-7}m^2$. Each electrode (surrounded by bubbles) is represented by one mesh node. The *in silico* model uses finite differences and standard relaxation techniques. The time step is $5.0\ 10^{-4}s$. The program was written in C++. The non-linear system of equations at anode and cathode boundaries was solved by Newton's method, using Multidimensional Root-Finding routines from the GNU Scientific Library (GSL).

## 3. Results and Discussion

Mathematical prediction of an optimal dose planning requires its validation with experimental results. With this goal in mind, we present predictions of ion transport mimicking the 3D gel EA/OPTED modeling previously discussed. We first show concentrations of the four ions considered ($H^+$, $OH^-$, $Cl^-$, $Na^+$) to illustrate the complex interaction and evolution during the electrolytic process. Ion transport is determinant for obtaining pH variations, which in turn are essential for reliable NTV prediction.

Figs. 2, 3 and 4 present model predictions of ion concentration and electric potential very close to the electrodes, over a line parallel to x-axis, anode and cathode are at positions ($1.242\ 10^{-2}m$, $1.15\ 10^{-2}m$) and ($1.058\ 10^{-2}m$, $1.15\ 10^{-2}m$) respectively, at 1200 $s$ and with an applied current of $4\ 10^{-3}A$. These results show that at the anode (right), protons increase, sodium, hydroxides and chloride decrease; at the cathode (left), hydroxides and sodium increase while protons and chloride diminish. It is noted that due to electrodes vicinity there are abrupt changes in concentrations in a zone close to electrodes. In particular, Fig. 4 shows the strong gradients of the protons giving rise to pH fronts. This is because, due to migration and diffusion, non-reacting cation (sodium) deplete at the anode and accumulate at the cathode, while protons and

**Table 2**
Proton diffusion coefficient fitted values ($D^{new}_{H^+} = D_{H^+}\ D_f$) and electrode effective area ($A_e$), for different electric currents (2, 4 and $8\ 10^{-3}A$, respectively). Last column gives the current density ($j_T$)

| $I\ [10^{-3}A]$ | $D_f$ | $A_e\ [10^{-5}\ m^2]$ | $j_T\ [10^2\ Am^{-2}]$ |
|---|---|---|---|
| 2 | 1.1 | 2 | 1 |
| 4 | 0.7 | 1 | 4 |
| 8 | 0.9 | 0.8 | 10 |

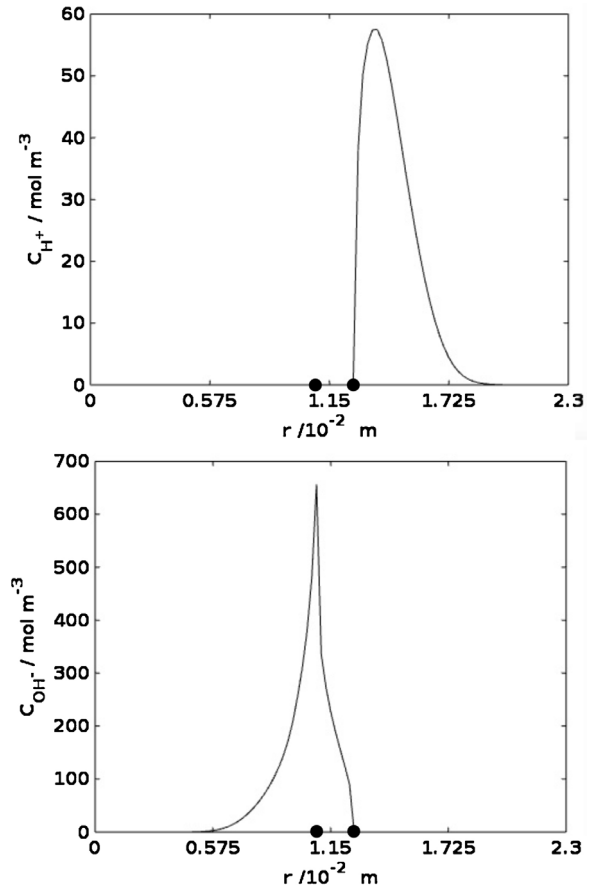


**Fig. 2.** Predicted $H^+$ (top) and $OH^-$ (bottom) concentrations vs. distance, at 1200 $s$ (I = $4\ 10^{-3}A$). Anode and cathode are located at ($1.242\ 10^{-2}m$, $1.15\ 10^{-2}m$) and ($1.058\ 10^{-2}m$, $1.15\ 10^{-2}m$), respectively, indicated by black circles.

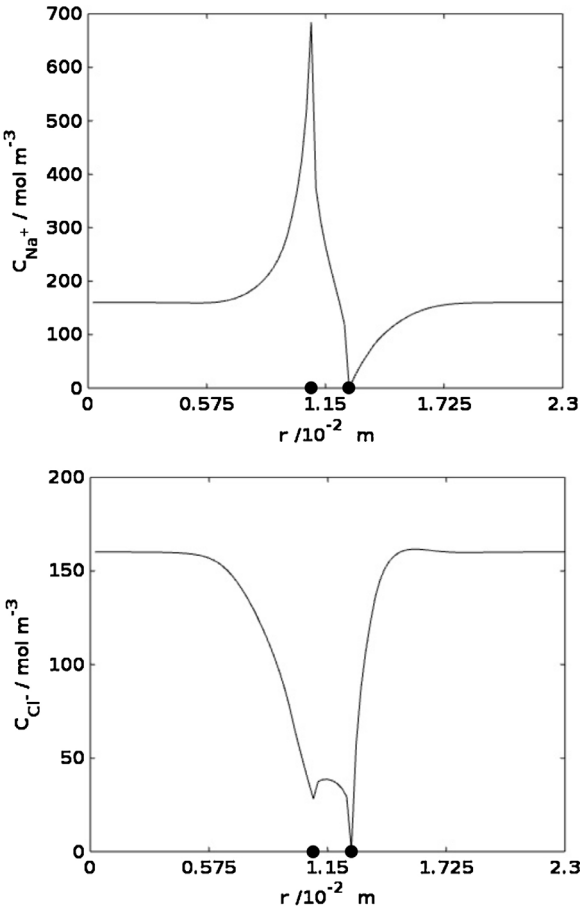


**Fig. 3.** Predicted $Na^+$ (top) and $Cl^-$ (bottom) concentrations vs. distance, at 1200 *s* (I = 4 $10^{-3}A$). Black circles indicate electrodes position.

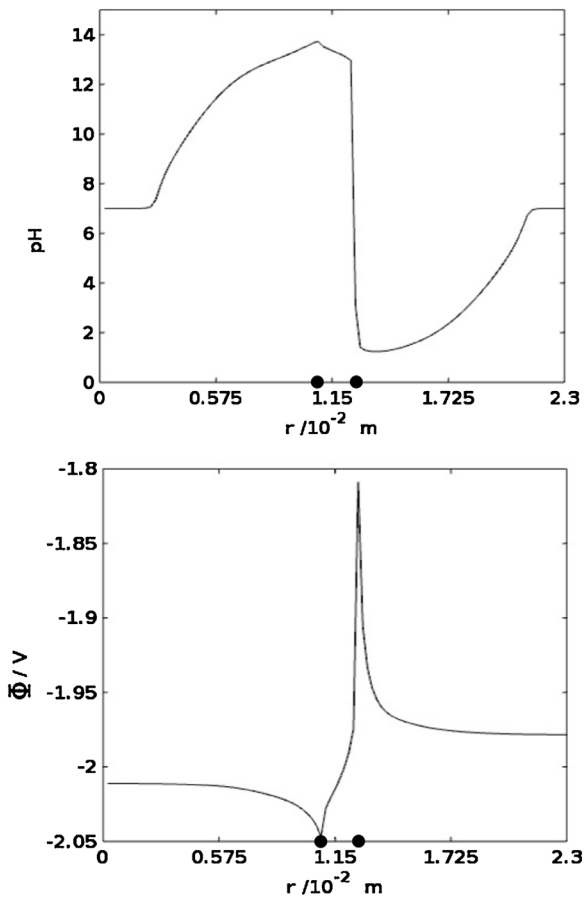


**Fig. 4.** Predicted *pH* variations (top) and electrostatic potential Φ (bottom) vs. distance, at 1200 *s* (I = 4 $10^{-3}A$). Black circles indicate electrodes position.

hydroxyl ions produced at electrodes are transported towards the periphery; between electrodes, they are neutralized yielding water. In turn, chlorides migrate from the cathode and are consumed at the anode to yield chlorine.

Fig. 5 shows a snapshot at 1200 *s* of the predicted electric field and the electrostatic potential for an electric current of 4 $10^{-3}A$. Image shows the strong variation of the electrostatic potential, and thus the electric field, near the electrodes and the asymmetry due to the influence of the difference between the acid and basic front velocities. Fig. 6, left column, shows *in vitro* results consisting in a time sequence of digital images seen from above and close to the electrodes. Fig. 6, right column, shows the predicted evolution of the acid (white circle) and basic (black circle) pH fronts. In both

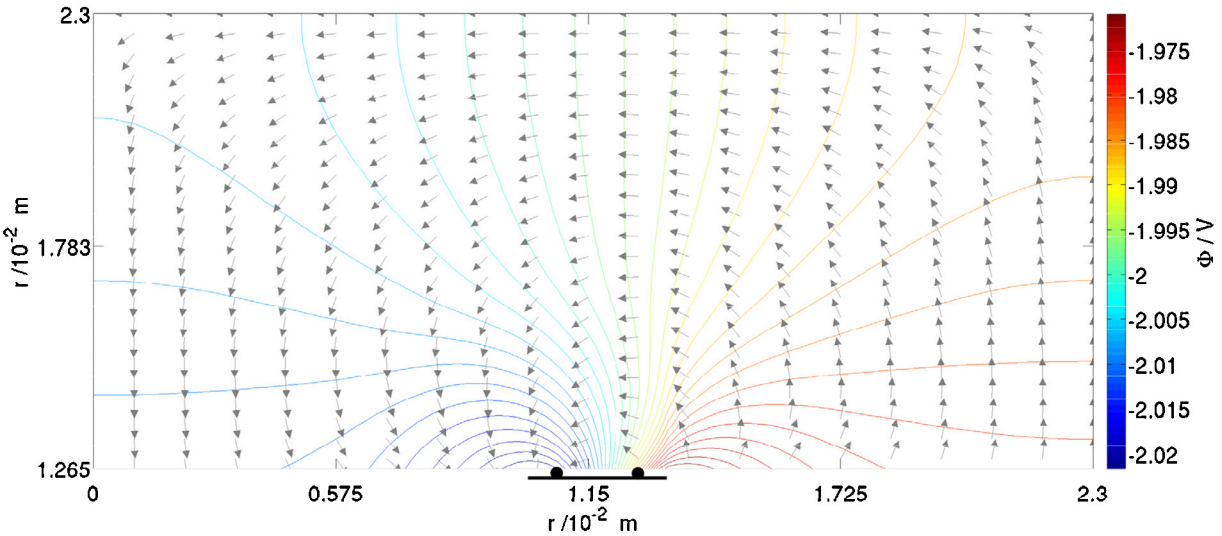


**Fig. 5.** Predicted electric field (arrows) at 1200 *s* (I = 4 $10^{-3}A$) and superposed, electrostatic potential Φ isolines. Black circles and line indicate electrodes and holder positions, respectively.

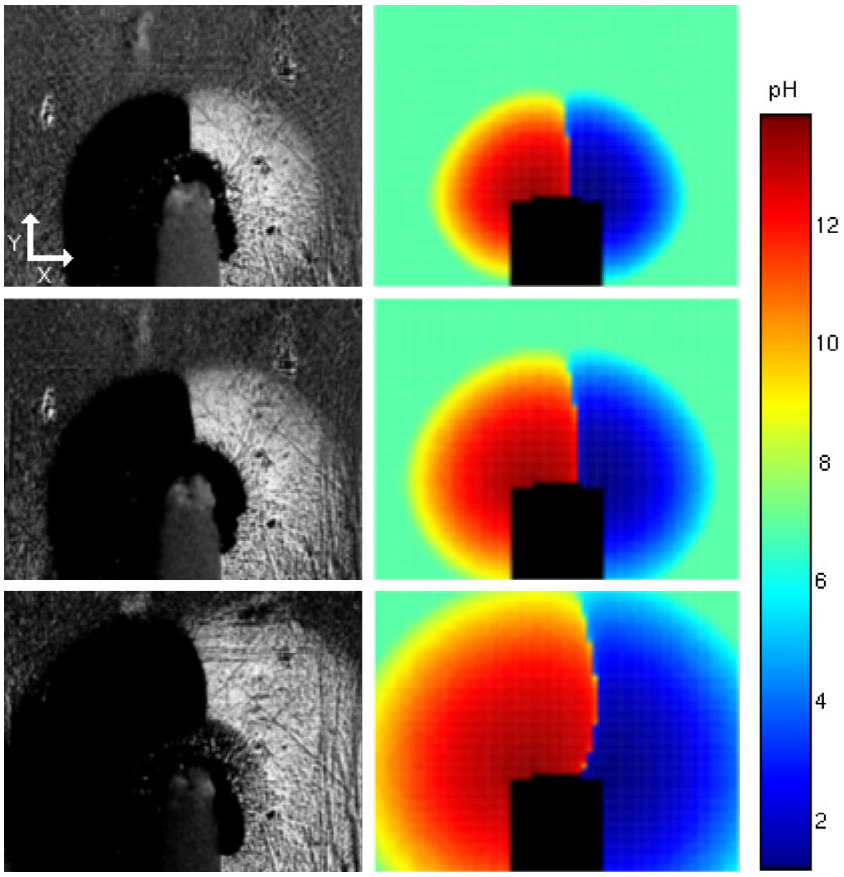


**Fig. 6.** Left column: *in vitro* time sequence of digital images (close to the OPTED electrodes) showing the evolution of the acid (white circle) and basic (black circle) pH fronts in a 3D gel model with I=4 $10^{-3}A$ (from top to down: 300 *s*, 700 *s* and 1200 *s*). The dark grey background corresponds to the gel matrix (figure taken from [19]). Right column: Predicted evolution of the acid (blue circle) and basic (red circle) pH fronts. The light green background corresponds to the gel matrix. Box dimensions: 1.29 $10^{-2}$ $m \times 1.65$ $10^{-2}$ $m$

figures (from top down) images are taken at: 300 *s*, 700 *s* and 1200 *s*. Box dimensions: 1.29 $10^{-2}$ $m \times 1.65$ $10^{-2}$ $m$. In the *in vitro* experiment, the dark grey background, as well as the small dark central halo, correspond to the gel matrix and bubbles generated at the electrodes, respectively. These bubbles have the effect of hindering pH front propagation near the electrodes and decreasing the electric current. In the *in silico* model predictions, the light green background corresponds to the gel matrix (there is a mismatch between the predicted and experimental pH fronts collision which is probably due to the fact that the halo seen in the experiments is not fully described in the *in silico* model).

Fig. 7, left: reslice from the time sequence of images (from Fig. 6, left column) showing the evolution of the acid (right) and basic (left) pH fronts. This reslice is constructed from a stack of pH spatial distributions over the same line as in Fig. 2, for different times, and then filtered with a border detection algorithm to show the trajectory of both fronts. It unveils the existence of significant pH gradients during the experiment. It is readily seen the larger extension of the anodic pH front relative to the cathodic one whose causes are discussed below. Fig. 7, right: predicted reslice from the time sequence of images showing the evolution of the acid (blue) and basic (red) pH fronts. Again, it is readily seen predictions following closely experimental measurements.

Fig. 8 shows *in vitro* results (black curves) and predictions (gray curves) of acid pH front trajectories, for different electric currents. Fig. 9 shows the same for basic pH fronts trajectories (thresholds for acid and basic pH fronts were $pH < 6.2$ and $pH > 8.0$, respectively). Results show that, as current intensity increases, at equal times trajectories cover a larger space. It is clearly seen that predictions

**Table 3**
Acid pH front trajectories (fitted with $r(t) = k * t^m$, where t is the application time, k and m are constants), for different electric currents (2, 4 and 8 $10^{-3}A$, respectively).

| $I$ | $k$ | $m$ |
|---|---|---|
| 2 $10^{-3}A$ | 0.00021713 | 0.4788 |
| 4 $10^{-3}A$ | 0.21485 | 0.50776 |
| 8 $10^{-3}A$ | 0.32039 | 0.48323 |

closely follow experiments. Moreover, acid pH fronts are faster than basic ones; this is due to the larger diffusion and migration coefficients of protons. Nevertheless, in all cases, acid and basic pH fronts advance is fitted by $r(t) = k * t^m$ where m is about 0.5 (see Table 3 and 4) which means that pH fronts scale in time as $t^{0.5}$, suggesting that pH fronts mainly follow a diffusion-controlled process.

In brief, our model predicts an initial neutral pH profile evolving into two half-spherical pH fronts, one basic and the other acid (from cathode and anode, respectively), expanding towards the periphery configuring a distorted full sphere. Due to the cathode-anode proximity the internal pH fronts rapidly coalesce and neutralize.

**Table 4**
Basic pH front trajectories (fitted with $r(t) = k * t^m$, where t is the application time, k and m are constants), for different electric currents (2, 4 and 8 $10^{-3}A$, respectively)

| $I$ | $k$ | $m$ |
|---|---|---|
| 2 $10^{-3}A$ | 0.20262 | 0.49363 |
| 4 $10^{-3}A$ | 0.2722 | 0.47258 |
| 8 $10^{-3}A$ | 0.34801 | 0.45272 |

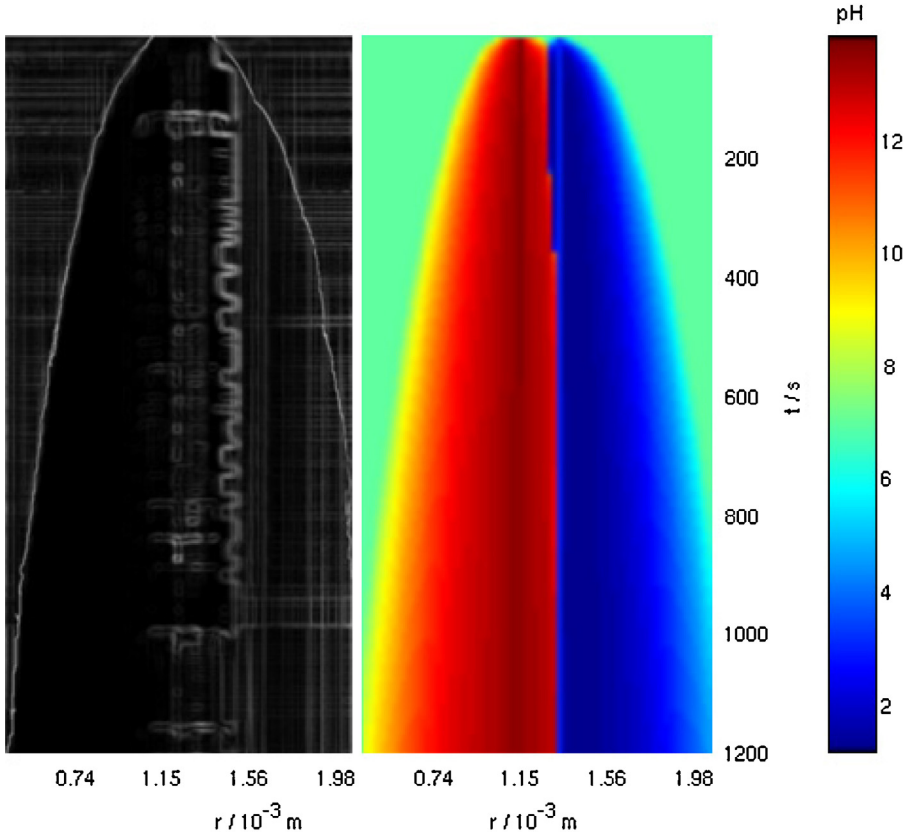


**Fig. 7.** Left:*in vitro* pH front tracking trajectories: acid (left) and basic (right) (figure taken from [19]); pH front trajectories is the result from a reslice of the time sequence of images from Fig. 6, left column, filtered with a border detection algorithm. Right: predicted pH front tracking trajectories.

These results show that model predictions closely follow *in vitro* measurements, in particular, predicted pH fronts. In this manner, we can safely conclude that our model has been satisfactorily validated with experimental results.

For dose planning methodology, we need to establish the coulomb dosage as a reliable dose parameter and to determine the optimal dose-response relationship between the coulomb dosage and NTV. Tissue destruction in EA is produced by the products emerging from the electrolysis process, in particular, pH fronts, which in turn, are a function of the coulomb dosage applied. In other words, in EA/OPTED, NTV is measured by the extent of tumor volume covered by pH fronts, thus there is a functional relation between NTV and the coulomb dosage applied. It follows consequently, that coulomb dosage stands as a reliable dose parameter as it controls the extension of the zones reached by the PH fronts.

The optimal dose-response relationship between the coulomb dosage and NTV for clinical use will be obtained with the help of previous mathematical results. To this end, we need to establish some basic assumptions. We first assume that the generic tumor to be ablated by the physician (plus a security margin) is contained in a sphere of radius R, thus a fixed volume size. We also assume that the OPTED electrode is located at the center of the tumor. Therefore, when this generic tumor is subjected to an EA/OPTED treatment its volume is gradually covered in time by a spherical pH front of radius r(I,t) that determines NTV. Clearly, when NTV reaches the sphere of radius R, the tumor is totally destroyed with a minimum coulomb dosage. This is exactly what happens in the 3D gel cube

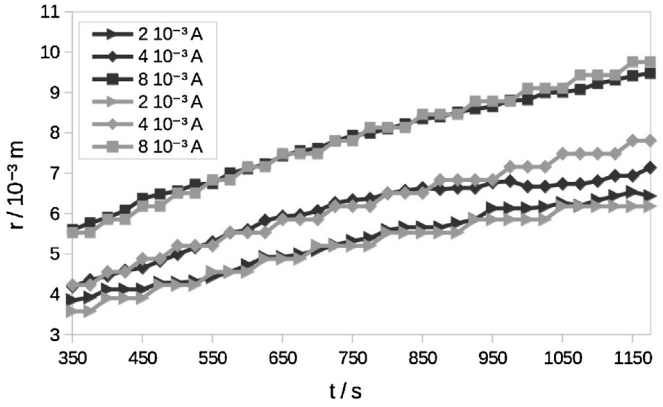


**Fig. 8.** Acid pH fronts vs. time, for different electric currents (black and gray curves represent *in vitro* and *in silico* results, respectively).

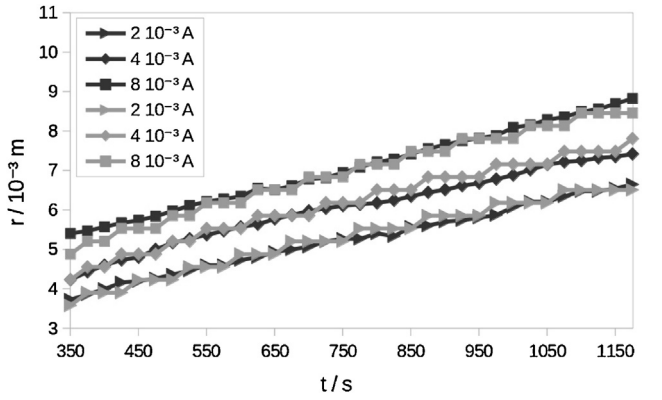


**Fig. 9.** Basic pH fronts vs. time, for different electric currents (black and gray curves represent *in vitro* and *in silico* results, respectively).

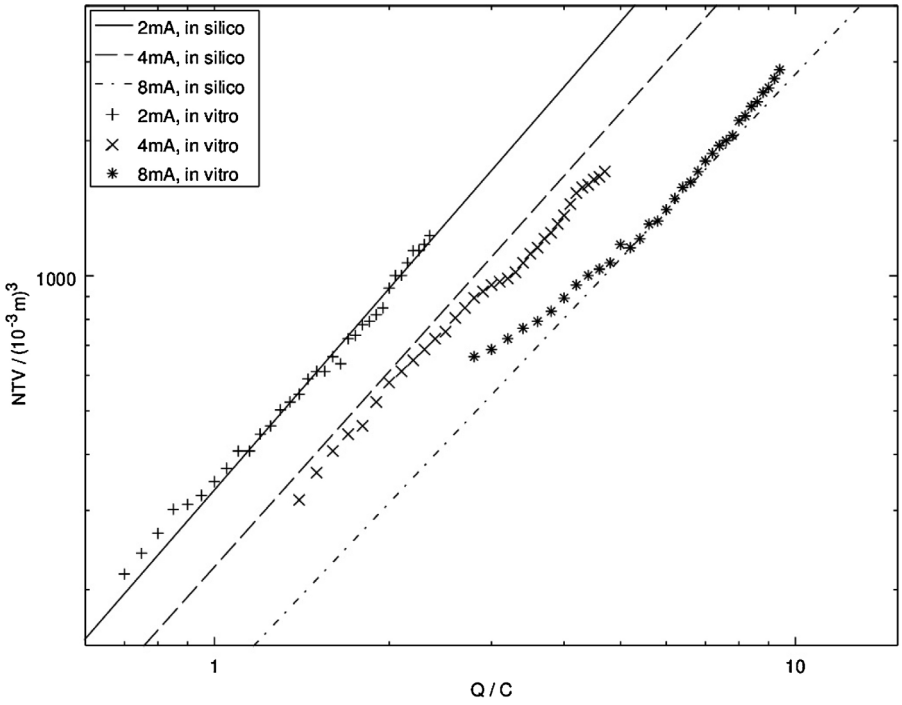


**Fig. 10.** Predicted (lines) and experimental (marker), respectively, NTV vs. coulomb dosage.

experiments assuming a tumor of radius R located in the center of the gel cube and constrained within the gel cube space. Based on these assumptions, and using *in silico* model results, Fig. 10 presents NTV theoretical predictions (straight lines) and experimental results (markers), respectively, as a function of the coulomb dosage. NTV is calculated as $NTV(Q) = a\,Q^b\,((10^{-3}m)^3)$ where a and b depend in the electric current: (a,b) pairs are ($1.25\,10^{-2}$,1.48), ($1.18\,10^{-2}$,1.42) and ($1.0510^{-2}$,1.36) for I=2, 4 and 8 $10^{-3}$ A, respectively. Results show that predictions follow experimental trends and there is a nonlinear relationship between NTV and coulomb dosage, that is, NTV scales as $Q^{1.4}$.

The accompanying graph in Fig. 11 presents theoretical predictions of NTV (lines of equal value) under an EA/OPTED as a function of the electric current ($I$) and time ($t$) of application. Here, NTV is calculated as $NTV(I,t)=(4/3)\pi\ r(I,t)^3\ ((10^{-3}m)^3)$ where the radius is fitted, from in silico results, with: $r(I,t)=(a+b\,I)t^{c-d\,I}$ and a, b, c and d take the value 0.16, 0.023, 0.5 and 0.007, respectively. The minimum current in Fig. 11 is 2 $10^{-3}$ A, which is the minimum value studied here; clearly, albeit lower values could in principle be applied, for sufficiently low currents no necrosis will take place because for a low rate of ion production at the electrodes, transport by diffusion will suffice to eliminate protons (at the anode) and hydroxyls (at the cathode), so as to avoid the rise of pH changes enough to destroy the tumor. Accordingly, given a tumor volume to be ablated, the physician can choose among different pairs of electric current and time of application, from the corresponding NTV

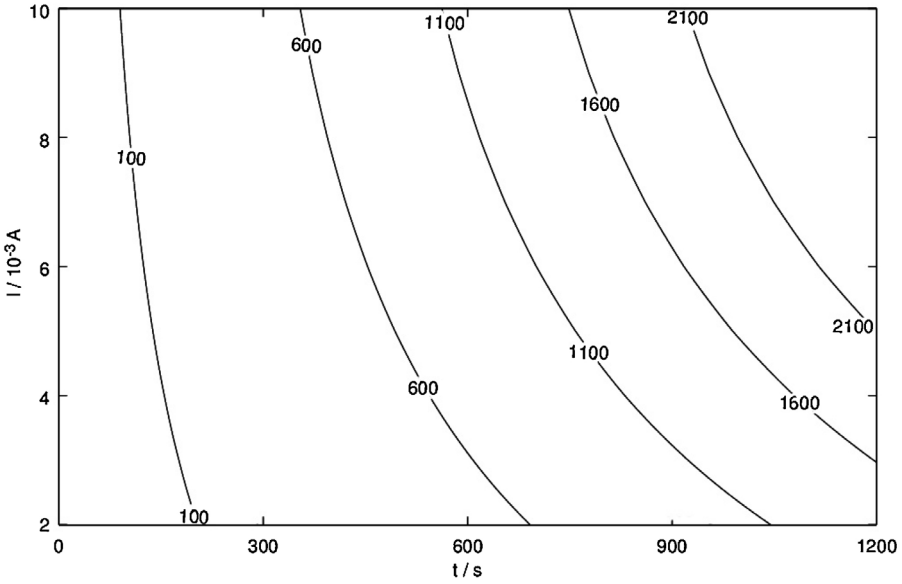


**Fig. 11.** Predicted lines of equal value of NTV ($(10^{-3}m)^3$) as a function of the electric current (I) vs. time (t) of application.

lines of equal value in Fig. 11. In particular, he may choose regarding patient conditions a low current and longer treatment time rather than a higher current and shorter treatment time, without inducing major secondary effects. In summary, given a tumor size and its characteristics, the EA/OPTED *in silico* model introduced here can predict the exact minimum coulomb dosage that would yield an optimum EA/OPTED protocol that is, maximizing NTV while minimizing healthy tissue damage.

## 4. Conclusions

Concerning dose planning methodology, it was established the coulomb dosage as a reliable dose parameter and it was determined the optimal dose-response relationship between the coulomb dosage and NTV, in the context of an EA/OPTED protocol for a given tumor size. The optimal EA/OPTED was defined as the optimal choice of the applied coulomb dosage that would succeed in achieving total NTV while minimizing healthy tissue damage. The optimal dose-response relationship was obtained by means of a mathematical model describing the ion transport underlying the electrolysis process. The basic assumption in EA/OPTED dose-response relationship is that the extent of NTV is determined by the extent of the volume covered by pH front spreading which in turn, is a function of the coulomb dosage. The mathematical model is based on the 2D Nernst-Planck equations for ion transport of four chemical species ($H^+$, $OH^-$, $Cl^-$, $Na^+$) under the assumption of electroneutrality and Butler-Volmer conditions at the electrodes interface. Theory predicts an initial neutral pH profile evolving into two half-spherical pH fronts, one basic and the other acid (from cathode and anode, respectively), expanding towards the periphery configuring a distorted full sphere. Due to the cathode-anode proximity the internal pH fronts rapidly coalesce and neutralize. *In silico* predictions closely follow *in vitro* measurements, in particular, areas covered by acid and basic fronts correlate well with necrotic areas, thus predicting the extension of NTV. Moreover, results show that the predicted relationship between NTV and coulomb dosage follows experimental trends, that is, NTV scales as $Q^{1.4}$ In conclusion, given a tumor size and characteristics, the EA/OPTED *in silico* model introduced here can predict the exact coulomb dosage that would yield an optimum EA/OPTED protocol.

## Acknowledgements

E. Luján has a scholarship from the Consejo Nacional de Investigaciones Científicas y Técnicas (CONICET); N. Olaiz, F. V. Molina, P. Turjanski and G. Marshall are researchers at CONICET. This work was supported by grants from CONICET (PIP 2012), Universidad de Buenos Aires (UBACyT 2014) and the International European Cooperation in Science and Technology (COST Action TD 1104). The funders had no role in the study, design, data collection, and analysis, decision to publish, or preparation of the manuscript.

## Appendix A.

### A.1. Boundary conditions

Using platinum electrodes the main reactions considered at the anode-tissue interface are oxygen evolution reaction and chlorine evolution reaction, respectively:

$$2H_2O \rightleftharpoons O_2 + 4H^+ + 4e^- \quad (R_{O_2})$$

$$2Cl^- \rightleftharpoons Cl_2 + 2e^- \quad (R_{Cl_2})$$

Mass transport of species $B$ across the anode surface ($\boldsymbol{N_B}\cdot\check{\boldsymbol{n}}$, where $\check{\boldsymbol{n}}$ is the normal vector to the surface) is either non-existent or equal to the charge transfer.

$$-D_{H^+}(\nabla C_{H^+}\cdot\check{\boldsymbol{n}}) - \frac{z_{H^+}}{|z_{H^+}|}u_{H^+}C_{H^+}(\nabla\Phi\cdot\check{\boldsymbol{n}}) = \frac{\nu_{H^+,R_{O_2}}}{n_{R_{O_2}}}\frac{\boldsymbol{j_{R_{O_2}}}\cdot\check{\boldsymbol{n}}}{F} \tag{14}$$

$$-D_{OH^-}(\nabla C_{OH^-}\cdot\check{\boldsymbol{n}}) - \frac{z_{OH^-}}{|z_{OH^-}|}u_{OH^-}C_{OH^-}(\nabla\Phi\cdot\check{\boldsymbol{n}}) = 0 \tag{15}$$

$$-D_{Cl^-}(\nabla C_{Cl^-}\cdot\check{\boldsymbol{n}}) - \frac{z_{Cl^-}}{|z_{Cl^-}|}u_{Cl^-}C_{Cl^-}(\nabla\Phi\cdot\check{\boldsymbol{n}}) = \frac{\nu_{Cl^-,R_{Cl_2}}}{n_{R_{Cl_2}}}\frac{\boldsymbol{j_{R_{Cl_2}}}\cdot\check{\boldsymbol{n}}}{F} \tag{16}$$

$$-D_{Na^+}(\nabla C_{Na^+}\cdot\check{\boldsymbol{n}}) - \frac{z_{Na^+}}{|z_{Na^+}|}u_{Na^+}C_{Na^+}(\nabla\Phi\cdot\check{\boldsymbol{n}}) = 0 \tag{17}$$

where $n_{R_{O_2}}$ and $n_{R_{Cl_2}}$ are the number of electrons transferred in the electrochemical reaction $R_{O_2}$ and $R_{Cl_2}$. $\nu_{H^+,R_{O_2}}$ and $\nu_{Cl_2,R_{Cl_2}}$ are the stoichiometric coefficients of species $H^+$ and $Cl_2$ in the reactions $R_{O_2}$ and $R_{Cl_2}$. $\boldsymbol{j_{R_{O_2}}}\cdot\check{\boldsymbol{n}}$ and $\boldsymbol{j_{R_{Cl_2}}}\cdot\check{\boldsymbol{n}}$ denote partial electric current density contributed by the electrochemical reactions $R_{O_2}$ and $R_{Cl_2}$ normal to the anode surface.

Using Butler-Volmer equation it is possible to compute the partial electric current density ($\boldsymbol{j_{R_{O_2}}}\cdot\check{\boldsymbol{n}}$) corresponding to oxygen evolution and proton release from electrochemical reaction $R_{O_2}$, normal to the anode surface:

$$\boldsymbol{j_{R_{O_2}}}\cdot\check{\boldsymbol{n}} = j^{eq}_{R_{O_2}}\left\{\exp\left[-\frac{F(\Phi+E^{eq}_{R_{O_2}})}{2RT}\right] - \left(\frac{P_{O_2}}{P^{eq}_{O_2}}\right)^{\frac{1}{4}}\left(\frac{C_{H^+}}{C^0_{H^+}}\right)\exp\left[\frac{F(\Phi+E^{eq}_{R_{O_2}})}{2RT}\right]\right\} \tag{18}$$

and the partial electric current density ($\boldsymbol{j_{R_{Cl_2}}}\cdot\check{\boldsymbol{n}}$) corresponding to chlorine evolution from electrochemical reaction $R_{Cl_2}$, normal to the anode surface:

$$\boldsymbol{j_{R_{Cl_2}}}\cdot\check{\boldsymbol{n}} = j^{eq}_{R_{Cl_2}}\left\{\left(\frac{C_{Cl^-}}{C^0_{Cl^-}}\right)\exp\left[-\frac{F(\Phi+E^{eq}_2)}{2RT}\right] - \left(\frac{P_{Cl_2}}{P^{eq}_{Cl_2}}\right)^{\frac{1}{2}}\exp\left[\frac{F(\Phi+E^{eq}_2)}{2RT}\right]\right\} \tag{19}$$

$j^{eq}_{R_{O_2}}$ and $j^{eq}_{R_{Cl_2}}$ denote the exchange of electric current density in the reactions $R_{O_2}$ and $R_{Cl_2}$ at equilibrium. $E^{eq}_{R_{O_2}}$ and $E^{eq}_{R_{Cl_2}}$ are the potential difference between solid and liquid phases at equilibrium conditions and relative to the standard electrode potential of the reactions $R_{O_2}$ and $R_{Cl_2}$.

$P^{eq}_{O_2}$, $P^{eq}_{Cl_2}$, $P^{eq}_{H_2}$ are the partial pressures of species $O_2$, $Cl_2$ and $H_2$ at equilibrium state. $C^0_{H^+}$, $C^0_{OH^-}$, $C^0_{Cl^-}$ are the initial concentrations of species $H^+$, $OH^-$ and $Cl^-$.

The ratio of a pressure and its equilibrium pressure is assumed to be 1:

$$\frac{P_{O_2}}{P^{eq}_{O_2}} = \frac{P_{Cl_2}}{P^{eq}_{Cl_2}} = \frac{P_{H_2}}{P^{eq}_{H_2}} = 1 \tag{20}$$

Total current density perpendicular to the anode surface ($\boldsymbol{j_T}\cdot\check{\boldsymbol{n}}$) is the sum of the partial current densities corresponding to both electrochemical reactions:

$$\boldsymbol{j_T}\cdot\check{\boldsymbol{n}} = \boldsymbol{j_{R_{O_2}}}\cdot\check{\boldsymbol{n}} + \boldsymbol{j_{R_{Cl_2}}}\cdot\check{\boldsymbol{n}} \tag{21}$$

Eqs. (9), (14) - (21) are used to obtain the concentrations of the four electrolytes analyzed ($H^+$, $OH^-$, $Cl^-$ and $Na^+$), the electric field and the electrostatic potential at the anode.

At the cathode-tissue interface the main reaction is:

$$2H_2O + 2e^- \rightleftharpoons H_2 + 2OH^- \quad (R_{H_2,2OH^-})$$

And the mass transport of species $B$ across the cathode surface ($\boldsymbol{N_B}\cdot\check{\boldsymbol{n}}$) is either non-existent or equal to the charge transfer.

$$-D_{H^+}(\nabla C_{H^+}\cdot\check{\boldsymbol{n}}) - \frac{z_{H^+}}{|z_{H^+}|}u_{H^+}C_{H^+}(\nabla\Phi\cdot\check{\boldsymbol{n}}) \quad = 0 \tag{22}$$

$$-D_{OH^-}(\nabla C_{OH^-}\cdot\check{\boldsymbol{n}}) - \frac{z_{OH^-}}{|z_{OH^-}|}u_{OH^-}C_{OH^-}(\nabla\Phi\cdot\check{\boldsymbol{n}}) = \frac{\nu_{OH^-,R_{H_2,2OH^-}}}{n_{H_2,2OH^-}}\frac{\boldsymbol{j_{R_{H_2,2OH^-}}}\cdot\check{\boldsymbol{n}}}{F} \tag{23}$$

$$-D_{Cl^-}(\nabla C_{Cl^-}\cdot\check{\boldsymbol{n}}) - \frac{z_{Cl^-}}{|z_{Cl^-}|}u_{Cl^-}C_{Cl^-}(\nabla\Phi\cdot\check{\boldsymbol{n}}) \quad = 0 \tag{24}$$

$$-D_{Na^+}(\nabla C_{Na^+}\cdot\check{\boldsymbol{n}}) - \frac{z_{Na^+}}{|z_{Na^+}|}u_{Na^+}C_{Na^+}(\nabla\Phi\cdot\check{\boldsymbol{n}}) \quad = 0 \tag{25}$$

The partial current density ($\boldsymbol{j_{R_{H_2,2OH^-}}}\cdot\check{\boldsymbol{n}}$) contributed by the hydrogen evolution and the hydroxide production reaction ($R_{H_2,2OH^-}$), and the total current density ($\boldsymbol{j_T}\cdot\check{\boldsymbol{n}}$), all normal to the cathode surface, are the same:

$$\boldsymbol{j_T}\cdot\check{\boldsymbol{n}} = \boldsymbol{j_{R_{H_2,2OH^-}}}\cdot\check{\boldsymbol{n}} \tag{26}$$

Eqs. (9), (22) - (26) are used to obtain the concentrations of the four electrolytes and the electrostatic potential at the cathode. $\boldsymbol{j_{R_{H_2,2OH^-}}}$ is a constant value (see Table 1).

At boundaries other than those where electrodes are located (walls and bubbles) the concentrations and potential gradients normal to the surface of the boundary are assumed to be zero:

$$\nabla C_{H^+}\cdot\check{\boldsymbol{n}} = \nabla C_{OH^-}\cdot\check{\boldsymbol{n}} = \nabla C_{Cl^-}\cdot\check{\boldsymbol{n}} = \nabla C_{Na^+}\cdot\check{\boldsymbol{n}} = \nabla\Phi\cdot\check{\boldsymbol{n}} = 0 \tag{27}$$

### A.2. Initial conditions

Regarding initial conditions, at $t$=0, concentrations are taken as constants in the entire electrolyte domain (initial salt concentration is set to be 160 $mol/m^3$, which are close to concentrations found in plasma and interstitial fluids [23]). Initial pH is set to be 7 (neutral). Initial electric potential at the anode surface, $\Phi^{t=0}_{anode}$, is computed through Eq. (21). Initial electric potential at the cathode surface, $\Phi^{t=0}_{cathode}$, is computed through an expression derived through the introduction of the concentration flux density at the cathode surface ($\boldsymbol{N_B}\cdot\check{\boldsymbol{n}}$) into Eq. (11):

$$\boldsymbol{E}\cdot\check{\boldsymbol{n}} = -\nabla\Phi\cdot\check{\boldsymbol{n}} = \frac{\boldsymbol{j_T}\cdot\check{\boldsymbol{n}}}{F\sum_B |z_B|u_B C_B} \tag{28}$$

Initial electric potential is computed via:

$$\Phi^{t=0}_{tissue} = 0.5 * (\Phi^{t=0}_{anode} + \Phi^{t=0}_{cathode}) \tag{29}$$

and the solution of the Laplace equation:

$$\nabla^2\Phi = 0 \tag{30}$$

With zero gradients at the remaining boundaries, i.e.,

$$\nabla\Phi\cdot\check{\boldsymbol{n}} = 0 \tag{31}$$

## References


[1] B. Nordenström, Biologically Closed Electrical Circuits: Clinical, Experimental and Theoretical Evidence for an Additional Circulatory System, Nordic Medical Publications, Stockholm, Sweeden, 1983.
[2] B. Nordenström, Am J Clin Oncol: Cancer Clinical Trials 12 (1989) 530.
[3] Y. Xin, Eur J Surg Suppl 574 (1994) 25.
[4] Y. Xin, D. Liu, X. Meng, Zhongguo Zhong Xi Yi Jie He Za Zhi 21 (2001) 174.
[5] D. Miklavčič, G. Serša, S. Novakovič, S. Rebersek, J Bioelectricity 9 (1990) 133.
[6] D. Miklavčič, G. Serša, M. Kryžanowski, S. Novakovič, F. Bobanovič, R. Golouh, L. Vodovnik, Bioelectrochem Bioenerg 30 (1993) 209.
[7] G. Serša, D. Miklavčič, Regional Cancer Treatment 6 (1993) 31.
[8] D. Miklavčič, A. Fajgelj, G. Serša, Bioelectrochem Bioenerg 35 (1994) 93.
[9] L. Mir, European Journal of Cancer Supp 4 (2006) 38.
[10] B. Mali, T. Jarm, M. Snoj, G. Sersa, D. Miklavcic, European Journal of Surgical Oncology 39 (2013) 4.
[11] M. Phillips, N. Raju, L. Rubinsky, B. Rubinsky, TECHNOLOGY 3 (2015) 1.
[12] E. Nilsson, J. Berendson, E. Fontes, Journal of Applied Electrochemistry 30 (2000) 1321.
[13] E. Nilsson, E. Fontes, Bioelectrochemisty 53 (2001) 213.
[14] E. Nilsson, H. von Euler, J. Berendson, A. Thörne, P. Wersäll, I. Näslund, A. Lagerstedt, K. Narfström, J. Olsson, Bioelectrochemistry 51 (2000) 1.
[15] E. Nilsson, J. Berendson, E. Fontes, J Electroanal Chem 460 (1999) 88.
[16] E. Nilsson, J. Berendson, E. Fontes, Bioelectrochem Bioenerg 47 (1998) 11.
[17] L. Colombo, G. González, G. Marshall, F. Molina, A. Soba, C. Suárez, P. Turjanski, Bioelectrochemistry 71 (2007) 223.
[18] P. Turjanski, N. Olaiz, P. Abou-Adal, C. Suárez, M. Risk, G. Marshall, Electrochimica Acta 54 (2009) 6199.
[19] N. Olaiz, F. Maglietti, C. Suárez, F. Molina, D. Miklavcicc, L. Mir, G. Marshall, Electrochimica Acta 55 (2010) 6010.
[20] E. Nilsson, Modelling of the electrochemical treatment of tumours, Ph.D. thesis, Department of Chemical Engineering and Technology, Applied Electrochemistry, Royal Institute of Technology (2000).
[21] Y.-l. Xin, F.-z. Xue, B.-s. Ge, F.-r. Zhao, B. Shi, W. Zhang, Bioelectromagnetics 18 (1997) 8.
[22] J. Newman, K. Thomas-Alyea, Electrochemical Systems, 3rd Edition, John Wiley & Sons, Inc, Hoboken, New Jersey, 2004.
[23] J. West, Physiological Basis of Medical Practice, 11th Edition, Lippincott, William & Wilkins, Baltimore, 1985.
[24] A. Damjanovic, V. Birss, D. Boudreaux, Journal of The Electrochemical Society 138 (1991) 2549.
[25] A. Bard, Encyclopedia of Electrochemistry of the Elements, Marcel Dekker, New York, 1973.
[26] W. Moore, Basic Physical Chemistry, Prentice-Hall Int Ed, London, 1983.